Chemical Engineering Journal 479 (2024) 147896

Contents lists available at ScienceDirect

Chemical Engineering Journal

journal homepage: www.elsevier.com/locate/cej

Fast synthesis of high-entropy oxides for lithium-ion storage

Ruiqi Ren [a,1], Yuwei Xiong [b,1], Zikang Xu [a], Jingyuan Zhang [a], Yizhou Zhang [a], Guoyin Zhu [a,*], Kuibo Yin [b,*], Shengyang Dong [a,c,*]

[a] *Institute of Advanced Materials and Flexible Electronics (IAMFE), School of Chemistry and Materials Science, Nanjing University of Information Science and Technology, Nanjing 210044, PR China*
[b] *SEU-FEI Nano-Pico Center, Key Laboratory of MEMS of Ministry of Education, Southeast University, Nanjing 210096, PR China*
[c] *Wuhan National Laboratory for Optoelectronics, Wuhan 430074, PR China*

ARTICLE INFO

Keywords:
High entropy oxides
Ultra-fast synthesis
Lithium-ion batteries
In-situ transmission electron microscopy

ABSTRACT

High-entropy oxides (HEOs) have been considered conspicuous battery materials due to their tunable properties and stable crystal structure. In this work, several kinds of high entropy oxides (HEOs) are prepared by an ultra-fast Joule heating method in several seconds. This simple and effective method enhances the efficiency of near four orders of magnitude than that of the common sintering methods. As anode materials of lithium-ion batteries (LIBs), they have considerable rate capacity and cycling stability. For example, quinary (MgCoNiCuZn)O HEO delivers a high capacity of ~150 mAh g^{-1} even at ultrahigh current density of 10 A g^{-1} and cycle stability up to 2,600 cycles. By in-situ transmission electron microscopy, the full lithiation/de-lithiation process is tracked down to the atomic scale in real time, observing the distinct reaction dynamics and structural evolutions in rock-salt-type (MgCoNiCuZn)O during cycling. Conversion/alloying reaction kinetics are identified by the disappearance of the original rock-salt phase and the formation of polyphase with the intercalation of lithium-ions. While upon de-lithiation, the post-lithiation polyphase state can be recovered to the original rock-salt-structured (MgCoNiCuZn)O. Our work provides valuable guidelines to high-efficient synthesis and mathematical understanding of lithium storage mechanisms of HEOs for next-generation long-life energy storage.

1. Introduction

Since the concept of “high entropy” was put forward, it has been aroused wide attention in the academic community because of its unique entropy stability. The first reported high entropy material (HEM) is high entropy alloy (HEA), which has been intensively studied in the decades since it was proposed in 2004 [1–3]. “High entropy” has been a hot area of research for materials design with complex components [4]. Up to now, various high-entropy materials have been proposed, such as high-entropy oxides, high-entropy diborides, high-entropy nitrides, high-entropy carbides, high-entropy fluorides, and high-entropy sulfides, etc. [5–13]. Among these HEMs, high entropy oxides (HEOs) have become a very notable HEM since it was proposed in 2015 [4]. As an emerging oxide system, like most HEMs, HEOs also have five or more different metal cations, whose molar ratios are close to each other. In addition, HEO also has a high configurational entropy (S_{config}), which is an important driving force for the formation of a stable single phase of all HEMs [14–16]. The S_{config} can be calculated by the Boltzmann equation:

$$S_{config} = -R\left[\left(\sum\nolimits_{i=1}^{N} x_i \ln x_i\right)_{cation-site} + \left(\sum\nolimits_{j=1}^{N} x_j \ln x_j\right)_{anion-site}\right] \tag{1}$$

where x_i and x_j represent the mole fraction of elements present in the cation and anion sites, respectively, and R is the gas constant. In effect, in HEOs, there are only oxygen anions, while there are five or more metal cations. Therefore, in the HEOs system, the entropy contribution of oxygen ions is negligible. Accordingly, the original equation can be reduced to the following form [17]:

$$S_{config} = -R\left(\sum\nolimits_{j=1}^{N} x_i \ln x_i\right)_{cation-site} \tag{2}$$

Generally, it is stipulated that when the configurational entropy is

---

[*] Corresponding authors at: Institute of Advanced Materials and Flexible Electronics (IAMFE), School of Chemistry and Materials Science, Nanjing University of Information Science and Technology, Nanjing 210044, PR China (S. Dong).

E-mail addresses: gyzhu@nuist.edu.cn (G. Zhu), yinkuibo@seu.edu.cn (K. Yin), dongsyst@nuist.edu.cn (S. Dong).

[1] These authors contributed equally to this work.

https://doi.org/10.1016/j.cej.2023.147896
Received 23 September 2023; Received in revised form 9 November 2023; Accepted 3 December 2023

greater than or equal to 1.5R, the oxide can be called HEOs [18].

On this basis, the complex element composition of HEOs can open-up huge possibilities as an excellent energy storage material. In the commercial field, LIBs have unshakable position in the portable equipment and electric vehicle industry [19–22]. In subsequent studies, HEOs, such as (MgCoNiCuZn)O, have been found to have great potential for applications as lithium storage materials [23–25]. However, most of the synthesis methods are time-consuming and energy-sucking. For example, Rost et al. chose to sinter raw materials at 1000 ℃ as long as 12 h [5]. Therefore, the further development of HEO synthesis methods has become an urgent issue. In this case, ultrafast high-temperature sintering (UHS) technology was developed. This method was first proposed by Wang et al. for the sintering of ceramics [26]. UHS is a sintering technology based on Joule's law. It uses the Joule thermal effect of the material or the carrier itself to generate a great deal of heat in an instant by applying a huge current in the conductor. Joule heating device can complete the heating behavior from room temperature to 3000 ℃ in a few seconds. The super rapid heating and super high-temperature upper limit are the most advanced highlights of the Joule thermal method, which reduces the preparation period of HEO from a dozen hours to several seconds, which is undoubtedly an explosive preparation process. Dong et al. first applied this method to synthesize (Mn, Fe, Co, Ni, Cu, Zn)$_3$O$_{4-x}$ HEO [27]. However, the crystal phase of the product is not pure. They believed that some easily reduced elements (such as Cu) in the raw material occurred in side reactions.

Herein, we seek to improve the synthesis of HEO by UHS technology in several seconds. According to the Gibbs free energy formula ($\Delta G = \Delta H - T\Delta S$), the high temperature and high entropy allow the reactants to obtain sufficient activation energy in a short time, which makes the reactants crystallize faster and better, forming a stable crystalline phase. The experimental results show that adjusting the calcination parameters solves the side reactions that may occur in the process of UHS of easily reduced elements. The as-prepared HEO, (MgCoNiCuZn)O, shows remarkable capacity and cycle stability. A high reversible capacity of ~525 mAh g^{-1} can be obtained at 50 mA g^{-1}. After 2,600 cycles at a high current density of 1 A g^{-1}, 80 % capacity retention is still achieved. By constructing nanoscale solid-state lithium-ion batteries in a TEM [28,29], we directly observed the structural and electrochemical reaction behaviors of (MgCoNiCuZn)O HEO upon lithiation/de-lithiation. We track conversion/alloying reaction upon the full lithiation, in which initial rock-salt-structured (MgCoNiCuZn)O disappear and then is converted to Co, Ni, Cu, MgO and Li$_{0.2}$Zn$_{0.8}$ polycrystalline dispersed in Li$_2$O matrix. While during the subsequent de-lithiation process, the poly crystalline phase can only be recovered to rock-salt-structured (MgCoNiCuZn)O, suggesting the symmetrical conversion reaction for the discharge–charge cycle, which corroborate the merits of (MgCoNiCuZn)O mentioned above. Importantly, this method is general, with which we have also successfully produce a series of HEOs: (MgCoNiMnZn)O, (FeCoNiCrMn)$_3$O$_4$, (FeCoNiMnTi)$_3$O$_4$, (FeCoNiMnCu)$_3$O$_4$, (MgCoNiCuZn)Fe$_2$O$_4$, (MgCoNiMnZn)Fe$_2$O$_4$, and so on.

2. Results and discussion

We used the first reported HEO, rock-salt (Mg$_{0.2}$Co$_{0.2}$Ni$_{0.2}$Cu$_{0.2}$Zn$_{0.2}$)O (designated as (MgCoNiCuZn)O), as a model material to evaluate the advanced nature of UHS and its anode application for lithium-ion batteries (LIBs). Compared with a classical calcination method of (MgCoNiCuZn)O (Fig. 1a), in which a long heating process is required (usually 2–5 ℃ min^{-1}) after intensive mixing to reach a relatively low-temperature level (about 1000 ℃) [30]. Meanwhile, the Joule heating method in this work will reduce the reaction time to ~3 s. A critical factor in reducing the length of the synthesis process is not only the ultra-fast heating rate, but also the ultra-high temperature that can be achieved. The recorded heating profile (temperature vs. time) of this work is shown in Fig. 1b, which demonstrates the ultra-fast heating/cooling rate and ultra-short sintering time. Fig. 1b also shows the relationship between temperature and time of UHS and conventional calcination synthesis. Traditional synthesis will take up to a dozen hours, whereas our method takes only 3 s, which shortens over 20,000 times. As mentioned above, explosive growth in synthesis efficiency is the most significant advantage of UHS over traditional methods. Using this advanced synthesis technology, we prepared a series of HEOs with rock-salt and spinel structures in 3–10 s, including rock-salt (MgCoNiCuZn)O, rock-salt (MgCoNiMnZn)O, spinel (FeCoNiCrMn)$_3$O$_4$, spinel (FeCoNiMnTi)$_3$O$_4$, spinel (FeCoNiMnCu)$_3$O$_4$, spinel (MgCoNiCuZn)Fe$_2$O$_4$, spinel (MgCoNiMnZn)Fe$_2$O$_4$, and so on.

As shown in Fig. 2a, X-ray diffraction (XRD) patterns demonstrate the raw materials have successfully turned to (MgCoNiCuZn)O HEO with high crystallinity in such a short sintering time (~3 s). The diffraction peaks are typical rock-salt structure and agreed with previous reports [15,31]. It should be noted that the impurity existed in previous report (such as some easily reduced elements like Cu) is solved in such ultra-fast preparation procedure. Fig. 1b shows the corresponding temperature profile of the fast Joule-heating method, which features an average holding temperature of ~1060 ℃. As presented in Fig. S1, we also collected the XRD data at others sintering temperature and sintering time. It can be demonstrated that 1060 ℃ and 3 s are the optimal sintering parameters. Scanning electron microscopy (SEM) image in Fig. S2 demonstrates that (MgCoNiCuZn)O HEO has an irregular particle morphology with a size distribution in the nanometer and micron range. The elemental energy-dispersive X-ray (EDX) spectroscopy mapping using a SEM shows that the distribution of various elements including Mg, Co, Ni, Cu, Zn, and O are uniform (Fig. 2b), which also demonstrates the highly uniform elemental mixing in (MgCoNiCuZn)O. As presented in Fig. 2c, the clear interplane spaces of 0.24 and 0.21 nm are the (1 1 1) and (2 0 0) planes of rock-salt-type (MgCoNiCuZn)O, respectively.

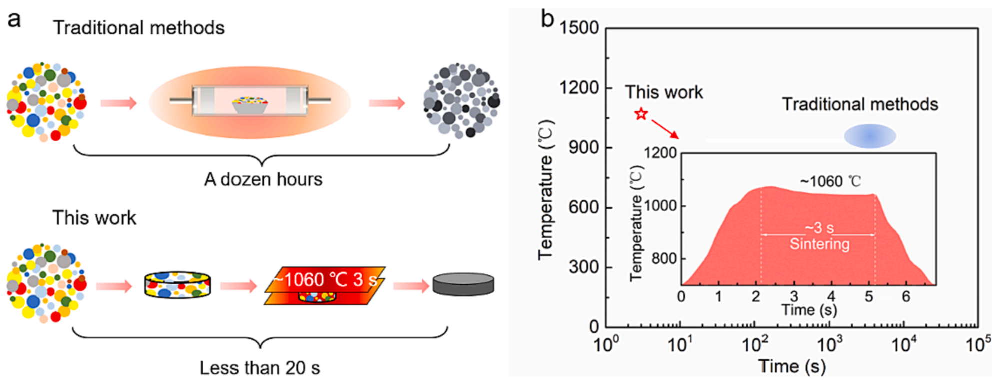

Fig. 1. Comparison between conventional syntheses and our approach. (a) The thumbnails of the conventional HEO synthetic process and our method. (b) Overwhelming advantages of UHS in terms of time and temperature. Inset: the recorded temperature profile of this work.

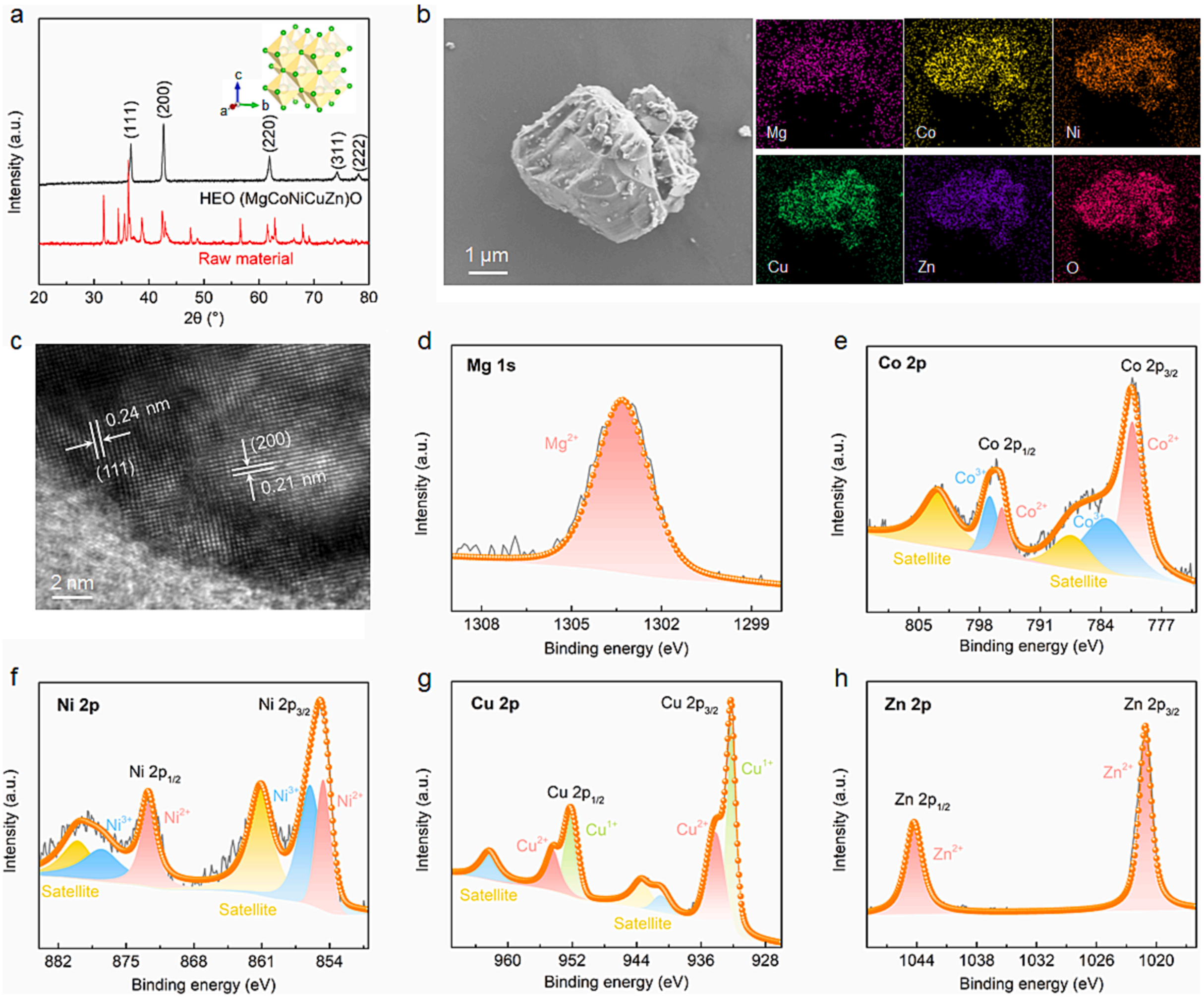

Fig. 2. The structure of (MgCoNiCuZn)O HEO. (a) XRD patterns of HEO and the corresponding raw materials. (b) SEM image and corresponding elemental mapping. (c) HRTEM image. (d-h) High-resolution XPS spectra of metal cations.

Because of the same proportion of cations in HEO and the divalent metal oxide in raw materials, the metal elements would, at first glance, appear to be 2 + state. However, the X-ray photoelectron spectroscopy (XPS) in Fig. 2d-h reveals that the valence states of the metals in the quinary HEO (i.e., Mg, Co, Ni, Cu, and Zn) are different. Co and Ni have valence states of both 2 + and 3+, partial Cu appear to be reduced to 1+, while Mg and Zn maintain the 2 + state.

Subsequently, a series of electrochemical characterizations were conducted to evaluate the potential application of (MgCoNiCuZn)O as lithium storage material. Fig. S3 presents the CV curves of (MgCoNiCuZn)O in the first 5 cycles with a scan rate of 2 mV s^{-1}. The first cycle is significantly larger than that of the subsequent cycles and an irreversible cathodic peak is detected around 0.4 V. This irreversible phenomenon which only appears in the first cycle is caused by the formation of solid electrolyte interphase (SEI) film. Fig. 3a depicts the galvanostatic charge–discharge (GCD) curves of (MgCoNiCuZn)O HEO between 0.01 and 3.00 V (vs. Li^+/Li, similarly hereinafter) at a current density of 50 mA g^{-1}. The high reversible capacity of ~525 mAh g^{-1} can be obtained with a low initial Coulombic efficiency of 50.3 %. This is mainly due to the capacity additionally contributed by the formation of SEI. However, the high Coulombic efficiency over 97 % can be provided since the second cycle. Notably, the GCD curves almost overlap from second to fifth cycles, which hints the high electrochemical reversibility of (MgCoNiCuZn)O HEO for lithium storage. The monotone GCD profiles instead of multiple redox plateaus, although five metal elements in (MgCoNiCuZn)O, connotes strong hybridization, perfect mixing, and internal redox among the quinary cations. During GCD cycles, the homogeneity of the quinary metal-ions in HEO anode was retained without phase separation. In addition, the (MgCoNiCuZn)O HEO also has a high-rate capacity. As shown in Fig. 3b and 3c, a respectable capacity of ~150 mAh g^{-1} can be provided at ultrahigh current density of 10 A g^{-1}. After rate testing from 0.05 to 10 A g^{-1}, the senary HEO recovers its high capacity at a low current density of 0.05 and 0.1 A g^{-1}. At the same time, to evaluate the cycle performance, we have carried out a long cycle charge–discharge test at a current density of 1 A g^{-1} (Fig. 3d). After 2,600 cycles, 80 % capacity retention is still achieved, which is an overwhelming majority of those have been reported metal oxides and HEO anode materials [25,32–34]. Notably, the morphology and structure of the HEO electrode did not change significantly after 200 cycles without cracks (Fig. S4). This can be explained by the ultra-high configurational entropy of HEO, which plays a crucial role in the structural stability during the long-term charge–discharge process [35]. Slight undulation occurs during the cycling test which is due to the changes in the ambient temperature. It is worth pointing out that we observed that, during the first several hundred cycles, the (MgCoNiCuZn)O electrode showed a trend of increasing specific capacity, which may be caused by the activation process during the charging and discharging process. This activation phenomenon can be demonstrated by electrochemical impedance spectroscopy (EIS). As shown in Fig. 3e, compared with the as-prepared electrode (Fig. 3e, black), a smaller semicircle can be found in the EIS spectra after 390 cycles (Fig. 3e, red). It confirms the enhanced conductivity (reduced charge transfer

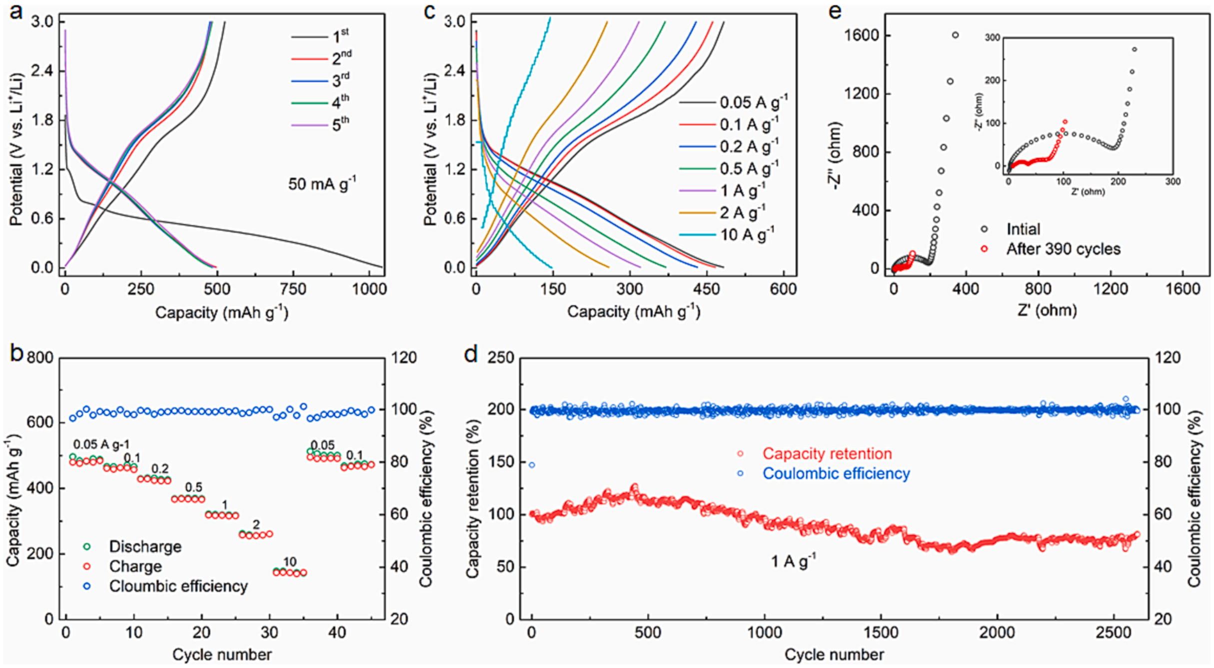

Fig. 3. Electrochemical performance of (MgCoNiCuZn)O HEO. (a) The first five galvanostatic charge–discharge curves at a current density of 50 mA g^{-1}. (b) Rate performance. (c) Typical charge–discharge curves from 0.05 to 10 A g^{-1}. (d) Long-term cycling test at 1 A g^{-1}. (e) EIS under the open circuit potential at the initial state and after 390 cycles.

impedance) during the first several hundred cycles. Notably, the additional semicircle in the high frequency region represents the impedance of the SEI film. We also test the cycling performance at a low current density of 0.1 A g^{-1}, which show stable cycling for 30 cycles without obvious capacity fading (Fig. S5).

To further describing the lithium storage behavior of (MgCoNiCuZn)O, we conduct more in-depth kinetic tests. Fig. 4a is the cyclic voltammetry (CV) curves of (MgCoNiCuZn)O at different scan rates, and we set the interval at 0.2–8 mV s^{-1}. It is universally acknowledged that a closed CV curve with a linear relationship between the area covered and the actual lithium storage capacity of the active material. Therefore, according to the content of the existing empirical formula, the peak current (i) and scan rate (v) conform to a power function [36–38]:

$$i = av^b \tag{3}$$

Among them, parameters a and b are adjustable, and the value range

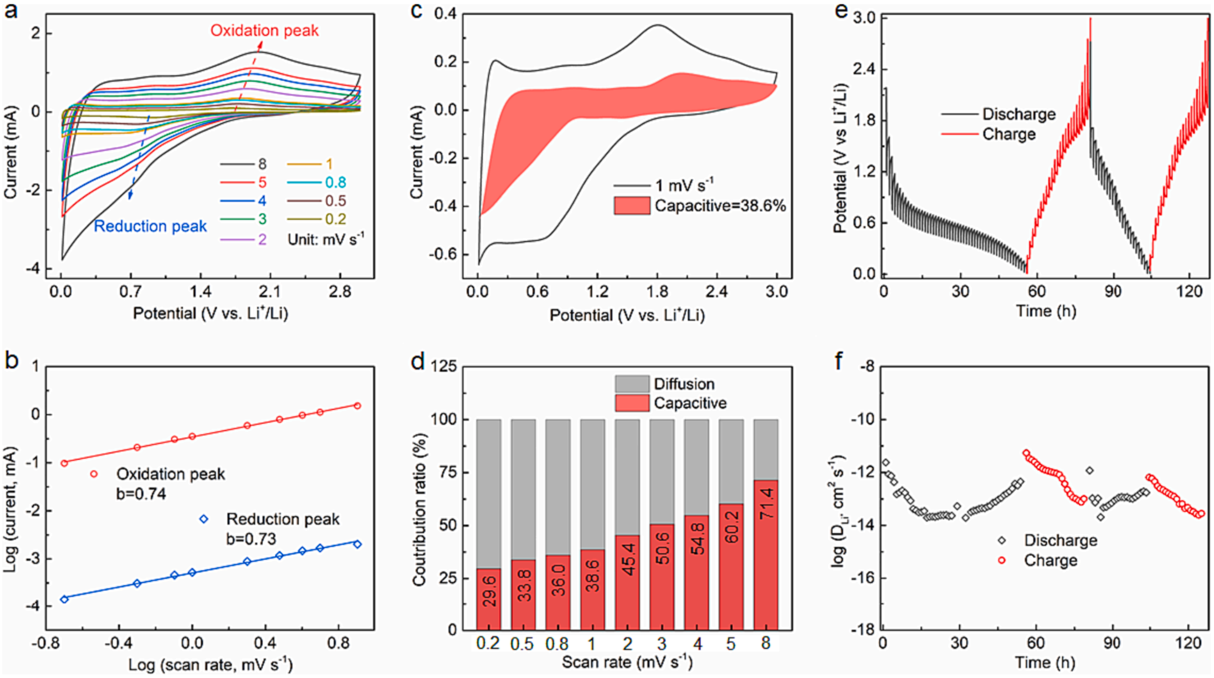

Fig. 4. Kinetic analysis of (MgCoNiCuZn)O HEO. (a) Cyclic voltammetry curves at different scan rates. (b) Linear fitting relationship between peak current and scan rates. (c) The capacitive contribution region at 1 mV s^{-1}. (d) Contribution ratio of capacitance at different scan rates. (e) The first two GITT curves and (f) the corresponding diffusion coefficient.

of *b* is 0.5–1. When *b* is 0.5, it indicates that the electrochemical process is diffusion controlled. Conversely, when *b* converges to 1, the main contribution to capacity is surface storage driven by non-diffusive capacitance. In this work, the *b* values of (MgCoNiCuZn)O are 0.74 and 0.73 (Fig. 4b) under the oxidation and reduction peaks, respectively, indicating that the charge storage is formed under the combination of diffusion control and non-diffusion control. Moreover, the capacity contribution rate of diffusion/non-diffusion can be roughly calculated by the following formula:

$$i = k_1 v + k_2 v^{\frac{1}{2}} \tag{4}$$

where k_1 and k_2 are the contribution rates of capacitance and diffusion, respectively. As shown in Fig. 4c and Fig. S6, we plot the detailed contribution region of capacitance behavior of (MgCoNiCuZn)O. It is obvious that the proportion of capacitance behavior increases significantly (from 29.6 % to 71.4 %) with the increase of scan rates from 0.2 to 8 mV s^{-1} (Fig. 4d). This indicates that the effect of capacitance behavior on the total capacity is strengthened at high scan rates. Furthermore, the diffusion kinetics was explored by galvanostatic intermittent titration technique (GITT). As presented in Fig. 4e, 4f and S7, the diffusion coefficient (D_{Li+}) values are between the orders of 10^{-13} and 10^{-11} cm^2 s^{-1}.

In the follow-up work, we also carried out the ex-situ XRD test to monitor the structural changes of HEO during lithium storage (Fig. S8). The results demonstrate that the diffraction peak of the original halite crystal phase of (MgCoNiCuZn)O gradually weakens and disappears later during the first lithiation process, and does not reappear in the subsequent de-lithiation and after 390 GCD cycles. To further explore the structure and phase evolution of (MgCoNiCuZn)O HEO during lithiation and de-lithiation, the all-solid-state nanosized LIBs that enables the in-situ electrochemical experiments was constructed in transmission electron microscopy (TEM, Titan 80–300) with PicoFemto STM-TEM holder, as schematically shown in Fig. 5a [39–42]. Once the Li_2O/Li electrode was in contact with the (MgCoNiCuZn)O HEO, the electrochemical lithiation process was initiated by applying a constant bias of − 10.0 V with respect to the Li_2O/Li electrode. Fig. 5b presents the panoramic TEM image of a single (MgCoNiCuZn)O nanoparticle before lithiation, which is directly attached to Li source. Upon applying a bias to the nanoparticle, the lithiation of (MgCoNiCuZn)O was immediately triggered from the point of contact with the Li source, accompanied by

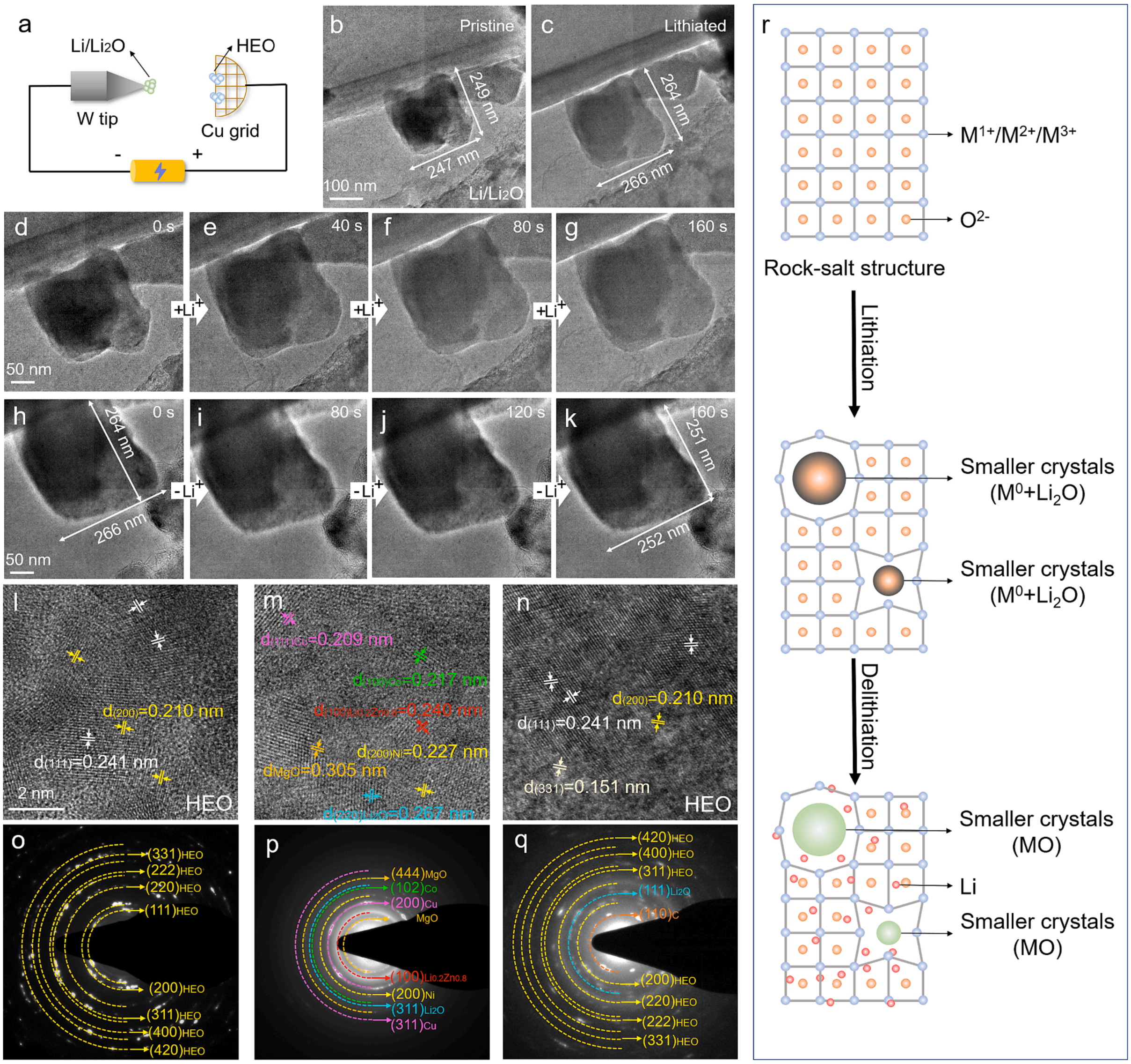

Fig. 5. In-situ TEM characterization of (MgCoNiCuZn)O HEO. (a) Schematic diagram of in-situ TEM setup. (b, c) HRTEM of pristine and after lithiation. (d-g) The morphological evolution during lithiation. (h-k) The morphological evolution during de-lithiation. HRTEM and ED for materials of the (i, o) pristine, (m, p) lithiation and (n, q) de-lithiation. (r) Schematic diagram of the structural transition of the lithiation/de-lithiation.

an obvious expansion along the x axes (247 to 266 nm) and y axes (249 to 264 nm) by ~7.7 % and ~6.0 %, respectively (Fig. 5b and 5c), which is a great improvement over the common metal oxide anodes (the volume expansion usually exceeds 100 %) [43–47]. The whole morphology evolution process of lithiation and de-lithiation was recorded as a series of TEM images, as shown in Fig. 5 (d-k). In addition to the volume expansion caused by lithiation, the extraction of lithium ions leads to the slight shrink along the x axes (266 nm to 252 nm) and y axes (264 nm to 251 nm) by ~5.3 % and ~4.9 %, respectively (Fig. 5h and 5 k). Notably, no visible crack or fracture is observed, indicating the reliable mechanical toughness during the whole lithiation/de-lithiation process. High-resolution TEM (HRTEM) images and electron diffraction (ED) patterns are used to identify the phase changes throughout the entire lithiation/de-lithiation process. As shown in Fig. 5l, the lattice spacings are measured to be 0.241 nm, 0.210 nm, corresponding to the rock-salt-structured (1 1 1) and (2 0 0) planes, respectively. Furthermore, the ED pattern corresponding to Fig. 5l is shown in Fig. 5o, which can be well indexed to different polycrystalline diffraction rings with (1 1 1), (2 0 0), (2 2 0), (3 1 1), (2 2 2), (4 0 0), (3 3 1) and (4 2 0) planes of rock-salt-structured (MgCoNiCuZn)O. As lithiation proceeded, the grains of Cu, Ni, Co, MgO, $Li_{0.2}Zn_{0.8}$ and Li_2O are formed, as evidenced by HRTEM image in Fig. 5m, in which the lattice distances of 0.209, 0.217, 0.227, 0.240, 0.267 and 0.305 nm can match well with the (1 1 1) plane of Cu (ICSD PDF #70–3038), the (1 0 0) plane of Co (ICSD PDF #89–7094), the (2 0 0) plane of Ni (ICSD PDF #89–7129), the (1 0 0) plane of $Li_{0.2}Zn_{0.8}$ (ICDD PDF#04–011-9312), the (2 2 0) plane of Li_2O (ICSD PDF #73–0593) and MgO (ICSD PDF #30–0794). Meanwhile, the emerging diffraction rings of Cu, Ni, Co, MgO, $Li_{0.2}Zn_{0.8}$ and Li_2O prove the occurrence of conversion/alloying reactions, as shown in Fig. 5p. With the complete extraction of Li^+ ions, the (MgCoNiCuZn)O can recover to initial morphology and phase, as demonstrate in Fig. 5n and 5q, which is also believed to be the reason for the excellent cyclic stability of (MgCoNiCuZn)O. The pattern in the center comes from (1 1 0) plane of C (ICSD PDF#22–1069), which is an essential part of the electrode. Comparing the characterization results of ex-situ XRD, we found that the more accurate HRTEM and ED detected the rock-salt phase that remained intact after the electrochemical reaction. Based on the above characterization results, a schematic of the reaction mechanism is illustrated in Fig. 5r. In the pristine state, (MgCoNiCuZn)O has a long-range ordered rock-salt phase. During the process of lithiation, the entry of Li induces some transition metal conversion reactions (e. g. $Co^{2+/3+}$, $Ni^{2+/3+}$, $Cu^{2+/1+}$, Zn^{2+}), while the other element (Mg^{2+}) that is inactive in this potential range plays a pivotal role in maintaining the stable matrix of the rock-salt structure. The HRTEM results visually show us that this conversion reaction occurs on a much smaller length scale (usually several nanometers). Naturally, after the end of de-lithiation, the previously reduced elements were refilled with the rock-salt matrix, completely restoring the structure. Moreover, the (MgCoNiCuZn)O electrode maintains the original rock-salt phase after 50 GCD cycles can be manifested by the corresponding HRTEM image and ED pattern in Fig. S9. In addition, we observed that SEI film (thickness of ~5 nm) was formed on the surface of (MgCoNiCuZn)O in the ex-situ TEM (Fig. S10), which further proved the reason for the low initial coulombic efficiency. Based on the analysis above, the redox reaction equation for charge and discharge should be as follows (Fig. 5r):

$$HEO+\frac{33}{20}Li\leftrightarrow\frac{1}{5}Co^{0}+\frac{1}{5}Cu^{0}+\frac{1}{5}Ni^{0}+\frac{1}{5}MgO+\frac{1}{20}LiZn_{4}+\frac{8}{5}Li_{2}O \qquad (5)$$

Importantly, we have also successfully synthesized a series of HEOs using UHS technology within 3 to 10 s (Fig. S11 and S12) including rock-salt structure (MgCoNiMnZn)O, and spinel structure $(FeCoNiCrMn)_3O_4$, $(FeCoNiMnTi)_3O_4$, $(FeCoNiMnCu)_3O_4$, $(MgCoNiCuZn)Fe_2O_4$, and $(MgCoNiMnZn)Fe_2O_4$. The detailed synthesis parameters can be found in Table S1. As shown in Fig. S13-S18, these HEOs possess considerable capacity, rate performance and cycling stability.

3. Conclusion

In summary, a series of HEOs with rock-salt and spinel structure were successfully synthesized by the UHS method. UHS has decisive advantages that other classical synthesis methods cannot achieve. We have reduced the synthesis time of HEOs from several hours to several seconds, which is certainly a significant leap. As an anode material for lithium storage, (MgCoNiCuZn)O HEO delivered high reversible capacity of 525 mAh g^{-1} and long cycle stability over 2,600 times. Through in-situ TEM observations including real-time HRTEM, ED tracking, we unveiled the conversion/alloying reaction mechanism during lithiation of (MgCoNiCuZn)O. It is unraveled that Co, Ni, Cu, MgO and $Li_{0.2}Zn_{0.8}$ poly crystalline have been ascertained as the final lithiation products and can be transformed back to the original rock-salt-structured (MgCoNiCuZn)O. The economical and effective preparation method and in-depth understanding of lithiation/de-lithiation process provide valuable guidelines of HEMs applications for next-generation high-performance batteries.

Declaration of competing interest

The authors declare that they have no known competing financial interests or personal relationships that could have appeared to influence the work reported in this paper.

Data availability

Data will be made available on request.

Acknowledgments

This work was supported by the National Natural Science Foundation of China (Grant Nos. 52102264 and 12174050), the Leading Edge Technology of Jiangsu Province (Grant No. BK20220009) and the Open Project Program of Wuhan National Laboratory for Optoelectronics (Grant No. 2020WNLOKF011).

Appendix A. Supplementary data

Supplementary data to this article can be found online at https://doi.org/10.1016/j.cej.2023.147896.

References

[1] L.J. Santodonato, Y. Zhang, M. Feygenson, C.M. Parish, M.C. Gao, R.J. Weber, J. C. Neuefeind, Z. Tang, P.K. Liaw, Deviation from high-entropy configurations in the atomic distributions of a multi-principal-element alloy, Nat. Commun. 6 (2015) 5964.

[2] P. Sarker, T. Harrington, C. Toher, C. Oses, M. Samiee, J.-P. Maria, D.W. Brenner, K.S. Vecchio, S. Curtarolo, High-entropy high-hardness metal carbides discovered by entropy descriptors, Nat. Commun. 9 (2018) 4980.

[3] M.C. Troparevsky, J.R. Morris, P.R. Kent, A.R. Lupini, G.M. Stocks, Criteria for predicting the formation of single-phase high-entropy alloys, Phys. Rev. X 5 (2015), 011041.

[4] B.L. Musicó, D. Gilbert, T.Z. Ward, K. Page, E. George, J. Yan, D. Mandrus, V. Keppens, The emergent field of high entropy oxides: Design, prospects, challenges, and opportunities for tailoring material properties, APL Mater. 8 (2020), 040912.

[5] M. Cui, C. Yang, B. Li, Q. Dong, M. Wu, S. Hwang, H. Xie, X. Wang, G. Wang, L. Hu, High-entropy metal sulfide nanoparticles promise high-performance oxygen evolution reaction, Adv. Energy Mater. 11 (2021), 2002887.

[6] J. Gild, Y. Zhang, T. Harrington, S. Jiang, T. Hu, M.C. Quinn, W.M. Mellor, N. Zhou, K. Vecchio, J. Luo, High-entropy metal diborides: a new class of high-entropy materials and a new type of ultrahigh temperature ceramics, Sci. Rep. 6 (2016) 1–10.

[7] T. Jin, X. Sang, R.R. Unocic, R.T. Kinch, X. Liu, J. Hu, H. Liu, S. Dai, Mechanochemical-assisted synthesis of high-entropy metal nitride via a soft urea strategy, Adv. Mater. 30 (2018), 1707512.

[8] L. Lin, K. Wang, A. Sarkar, C. Njel, G. Karkera, Q. Wang, R. Azmi, M. Fichtner, H. Hahn, S. Schweidler, High-entropy sulfides as electrode materials for Li-ion batteries, Adv. Energy Mater. 12 (2022) 12.

[9] C.R. Mccormick, R.E. Schaak, Simultaneous Multication exchange pathway to high-entropy metal sulfide nanoparticles, J. Am. Chem. Soc. 143 (2021) 1017.

[10] C.M. Rost, E. Sachet, T. Borman, A. Moballegh, E.C. Dickey, D. Hou, J.L. Jones, S. Curtarolo, J.-P. Maria, Entropy-stabilized oxides, Nat. Commun. 6 (2015) 8485.

[11] T. Wang, Z. Chen, J. Yang, S.D. Liang, High-entropy perovskite fluorides: A new platform for oxygen evolution catalysis, J. Am. Chem. Soc. 142 (2020) 4550–4554.

[12] J. Zhou, J. Zhang, F. Zhang, B. Niu, L. Lei, W. Wang, High-entropy carbide: A novel class of multicomponent ceramics, Ceram. Int. 44 (2018) 22014.

[13] P.A. Sukkurji, Y. Cui, S. Lee, K. Azmi, R. Wang, A. Sarkar, S. Indris, S. S. Bhattacharya, R. Kruk, H. Hahn, Mechanochemical synthesis of novel rutile-type high entropy fluorides for electrocatalysis, J. Mater. Chem. A 9 (2021) 8998–9009.

[14] M. Fracchia, M. Coduri, M. Manzoli, P. Ghigna, U.A. Tamburini, Is configurational entropy the main stabilizing term in rock-salt Mg0.2Co0.2Ni0.2Cu0.2Zn0.2O high entropy oxide? Nat. Commun. 13 (2022) 2977.

[15] X. Liu, Y. Xing, K. Xu, H. Zhang, M. Gong, Q. Jia, S. Zhang, W. Lei, Kinetically accelerated lithium storage in high-entropy (LiMgCoNiCuZn)O enabled by oxygen vacancies, Small 18 (2022), 2200524.

[16] Y. Zhang, T.T. Zuo, Z. Tang, M.C. Gao, K.A. Dahmen, P.K. Liaw, Z.P. Lu, Microstructures and properties of high-entropy alloys, Prog. Mater. Sci. 61 (2014) 1–93.

[17] L.A. Xiang, A. Jm, A. Kc, B. Cl, C. Xz, D. La, Design and investigate the electrical properties of Pb(Mg0.2Zn0.2Nb0.2Ta0.2W0.2)O3–PbTiO3 high-entropy ferroelectric ceramics, Ceram. Int. 48 (2022) 12848.

[18] B. Murty, J. Yeh, S. Ranganathan, High Entropy Alloys, Butterworth-Heinemann Ltd (Verlag). 2014.

[19] S. Dong, N. Lv, Y. Wu, G. Zhu, X. Dong, Lithium-ion and sodium-ion hybrid capacitors: from insertion-type materials design to devices construction, Adv. Funct. Mater. 31 (2021) 2100455.

[20] S. Dong, Y. Wang, C. Chen, L. Shen, X. Zhang, Niobium tungsten oxide in a green water-in-salt electrolyte enables ultra-stable aqueous lithium-ion capacitors, Nano-Micro Lett. 12 (2020) 1–11.

[21] S. Dong, Y. Xu, L. Wu, H. Dou, X. Zhang, Surface-functionalized graphene-based quasi-solid-state Na-ion hybrid capacitors with excellent performance, Energy Storage Mater. 11 (2018) 8–15.

[22] A.E. Abdelmaoula, L. Du, L. Xu, Y. Cheng, A.A. Mahdy, M. Tahir, Z. Liu, L. Mai, Biomimetic brain-like nanostructures for solid polymer electrolytes with fast ion transport, Sci. China Mater 65 (2022) 1476–1484.

[23] A. Sarkar, L. Velasco, D. Wang, Q. Wang, G. Talasila, L. de Biasi, C. Kübel, T. Brezesinski, S.S. Bhattacharya, H. Hahn, High entropy oxides for reversible energy storage, Nat. Commun. 9 (2018) 3400.

[24] D. Wang, S. Jiang, C. Duan, J. Mao, Y. Dong, K. Dong, Z. Wang, S. Luo, Y. Liu, X. Qi, Spinel-structured high entropy oxide (FeCoNiCrMn)3O4 as anode towards superior lithium storage performance, J. Alloy. Compd. 844 (2020), 156158.

[25] B. Xiao, G. Wu, T. Wang, Z. Wei, Y.B. Sui, J. Shen, F. Qi, J Zheng Wei, High-entropy oxides as advanced anode materials for long-life lithium-ion batteries, Nano Energy 95 (2022), 106962.

[26] Y.-X. Gong, J.-J. Wang, Solid-state batteries: from fundamental interface characterization to realize sustainable promise, Rare Metals 39 (2020) 743–744.

[27] Q. Dong, M. Hong, J. Gao, T. Li, M. Cui, S. Li, H. Qiao, A.H. Brozena, Y. Yao, X. Wang, Rapid synthesis of high-entropy oxide microparticles, Small 18 (2022), 2104761.

[28] L. Zhao, H.-H. Wu, C. Yang, Q. Zhang, G. Zhong, Z. Zheng, H. Chen, J. Wang, K. He, B. Wang, T. Zhu, X. Zeng, M. Liu, M.-S. Wang, Mechanistic Origin of the High Performance of Yolk@Shell Bi_2S_3@N-Doped Carbon Nanowire Electrodes, ACS Nano 12 (2018) 12597.

[29] J. Sun, Y. Cheng, H. Zhang, X. Yan, Z. Sun, W. Ye, W. Li, M. Zhang, H. Gao, J. Han, D.-L. Peng, Y. Yang, M.-S. Wang, Enhanced cyclability of lithium metal anodes enabled by anti-aggregation of lithiophilic Seeds, Nano Lett. 22 (2022) 5874.

[30] N. Qiu, H. Chen, Z. Yang, S. Sun, Y. Wang, Y. Cui, A high entropy oxide (Mg0.2Co0.2Ni0.2Cu0.2Zn0.2O) with superior lithium storage performance, J. Alloy. Compd. 777 (2019) 767.

[31] C. Triolo, W. Xu, B. Petrovičovà, N. Pinna, S. Santangelo, Evaluation of entropy-stabilized (Mg0.2Co0.2Ni0.2Cu0.2Zn0.2)O oxides produced via solvothermal method or electrospinning as anodes in lithium-ion batteries, Adv. Funct. Mater. 32 (2022) 2202892.

[32] H. Wei, H.-Y. Yang, X.-Q. Zhang, J.-F. Zhu, P.-P. Qiu, W. Luo, Hydrogen peroxide enabled two-dimensional molybdenum trioxide nanosheet clusters for enhanced surface Li-ion storage, Tungsten 3 (2021) 338–347.

[33] L. Su, J. Ren, T. Lu, K. Chen, J. Ouyang, Y. Zhang, X. Zhu, L. Wang, H. Min, W. Luo, Z. Sun, Q. Zhang, Y. Wu, L. Sun, L. Mai, F. Xu, Deciphering structural origins of highly reversible lithium storage in high entropy oxides with in situ transmission electron microscopy, Adv. Mater. 35 (2023), 2205751.

[34] O.J. Marques, C. Chen, E.V. Timofeeva, C.U. Segre, Local structure and conversion chemistry of high-entropy oxides as Li-ion anodes, J. Power Sources 564 (2023), 232852.

[35] G. Anand, A. P. Wynn, C. M. Handley, C. L. Freeman, Phase stability and distortion in high-entropy oxides. Acta Mater. 146(2018,), 119.

[36] Z. Zhang, B. Xi, X. Wang, X. Ma, W. Chen, J. Feng, S. Xiong, Oxygen defects engineering of $VO_2\cdot xH_2O$ nanosheets via in situ polypyrrole polymerization for efficient aqueous zinc ion storage, Adv. Funct. Mater. 31 (2021), 2103070.

[37] Y. Zhang, P. Chen, Q. Wang, Q. Wang, K. Zhu, K. Ye, G. Wang, D. Cao, J. Yan, Q. Zhang, High-capacity and kinetically accelerated lithium storage in MoO3 enabled by oxygen vacancies and heterostructure, Adv. Energy Mater. 11 (2021), 2101712.

[38] Y. Shen, Y. Jiang, Z. Yang, J. Dong, W. Yang, Q. An, L. Mai, Electronic structure modulation in MoO_2/MoP heterostructure to induce fast electronic/ionic diffusion kinetics for lithium storage, Adv. Sci. 9 (2022) 2104504.

[39] Y. Wen, M. Zhu, S. Song, L. Xin, Y. Xiong, J. Li, Y. Shen, K. Yin, L. Sun, In situ TEM investigation of large crystal formation in lithiated SnO_2 anode assisted by electron beam irradiation, J. Mater. Chem. A 9 (2021) 22301–22312.

[40] R. Fu, J. Pan, M. Wang, H. Min, H. Dong, R. Cai, Z. Sun, Y. Xiong, F. Cui, S.-Y. Lei, S. Chen, J. Chen, L. Sun, Q. Zhang, F. Xu, In situ atomic-scale deciphering of multiple dynamic phase transformations and reversible sodium storage in ternary metal sulfide anode, ACS Nano 17 (2023) 12483–12498.

[41] L. Yao, W. Xia, H. Zhang, H. Dong, H.L. Xin, P. Gao, R. Cai, C. Zhu, Y. Wu, M. Nie, S. Lei, L. Sun, F. Xu, In situ visualization of sodium transport and conversion reactions of FeS_2 nanotubes made by morphology engineering, Nano Energy 60 (2019) 424–431.

[42] W. Ye, F. Pei, X. Lan, Y. Cheng, X. Fang, Q. Zhang, N. Zheng, D.-L. Peng, M.-S. Wang, Stable nano-encapsulation of lithium through seed-free selective deposition for high-performance li battery anodes, Adv. Energy Mater. 10 (2020) 1902956.

[43] J.F.S. Fernando, C. Zhang, K.L. Firestein, J.Y. Nerkar, D.V. Golberg, ZnO quantum dots anchored in multilayered and flexible amorphous carbon sheets for high performance and stable lithium ion batteries, J. Mater. Chem. A 7 (2019) 8460–8471.

[44] S. Jia, Y. Wang, X. Liu, S. Zhao, W. Zhao, Y. Huang, Z. Li, Z. Lin, Hierarchically porous CuO nano-labyrinths as binder-free anodes for long-life and high-rate lithium-ion batteries, Nano Energy 59 (2019) 229–236.

[45] V. Soundharrajan, B. Sambandam, J. Song, S. Kim, J. Jo, P.T. Duong, S. Kim, V. Mathew, J. Kim, Metal organic framework-combustion: a one-pot strategy to NiO nanoparticles with excellent anode properties for lithium ion batteries, J. Energy Chem. 27 (2018) 300–305.

[46] H. Zhang, C. Wang, H.-L. Sun, G. Fu, S. Chen, Y.-J. Zhang, B.-H. Chen, J.R. Anema, Z.-L. Yang, J.-F. Li, Z.-Q. Tian, In situ dynamic tracking of heterogeneous nanocatalytic processes by shell-isolated nanoparticle-enhanced Raman spectroscopy, Nat. Commun. 8 (2017) 15447.

[47] G. Zhong, K. Qu, C. Ren, Y. Su, B. Fu, M. Zi, L. Dai, Q. Xiao, J. Xu, X. Zhong, F. An, M. Ye, S. Ke, S. Xie, J. Wang, P. Gao, J. Li, Epitaxial array of Fe_3O_4 nanodots for high rate high capacity conversion type lithium ion batteries electrode with long cycling life, Nano Energy 74 (2020), 104876.